Return to the Forgotten Ultraluminous X-Ray Source: A Broadband NICER+NuSTAR Study of NGC 4190 ULX-1

Hannah P. Earnshaw[1] , Matteo Bachetti[2] , Murray Brightman[1] , Felix Fürst[3] , Fiona A. Harrison[1] , Matthew Middleton[4] ,
Renee Ludlam[5] , Sean N. Pike[6] , Daniel Stern[7] , and Dominic J. Walton[8]

[1] Cahill Center for Astronomy and Astrophysics, California Institute of Technology, Pasadena, CA 91125, USA; hpearn@caltech.edu
[2] NAF-Osservatorio Astronomico di Cagliari, Selargius (CA), Italy
[3] European Space Astronomy Centre (ESAC), Science Operations Department, 28692, Villanueva de la Cañada, Madrid, Spain
[4] School of Physics & Astronomy, University of Southampton, Southampton, Southampton SO17 1BJ, UK
[5] Department of Physics & Astronomy, Wayne State University, 666 West Hancock Street, Detroit, MI 48201, USA
[6] Department of Astronomy & Astrophysics, University of California, San Diego, 9500 Gilman Drive, La Jolla, CA 92093, USA
[7] Jet Propulsion Laboratory, California Institute of Technology, 4800 Oak Grove Drive, Pasadena, CA 91109, USA
[8] Centre for Astrophysics Research, University of Hertfordshire, College Lane, Hatfield AL10 9AB, UK

Abstract

We observed the nearby and relatively understudied ultraluminous X-ray source (ULX) NGC 4190 ULX-1 jointly with Neutron Star Interior Composition Explorer (NICER) and NuSTAR to investigate its broadband spectrum, timing properties, and spectral variation over time. We found NGC 4190 ULX-1 to have a hard spectrum characterized by two thermal components (with temperatures $\sim$0.25 and $\sim$1.6 keV) and a high-energy excess typical of the ULX population although the spectrum turns over at an unusually low energy. While no pulsations were detected (with pulsed fraction 3σ upper limits of 16% for NICER and 35% for NuSTAR), the source shows significant stochastic variability, and the covariance spectrum indicates the presence of a high-energy cutoff power-law component, potentially indicative of an accretion column. Additionally, when fitting archival XMM-Newton data with a similar model, we find that the luminosity–temperature evolution of the hot thermal component follows the behavior of a super-Eddington slim disk though the expected spectral broadening for such a disk is not seen, suggesting that the inner accretion disk may be truncated by a magnetic field. Therefore, despite the lack of detected pulsations, there is tantalizing evidence for NGC 4190 ULX-1 being a candidate neutron star accretor although further broadband observations will be required to confirm this behavior.

1. Introduction

It is now widely agreed that ultraluminous X-ray sources (ULXs; defined as extragalactic nonnuclear point sources with X-ray luminosity $>10^{39}$ erg s^{-1}) are a population primarily made up of stellar-mass compact objects accreting at super-Eddington rates, giving them their distinctive high luminosities and particular spectral shapes (for recent reviews, see King et al. 2023; Pinto & Walton 2023). Key to this discovery initially were high-quality XMM-Newton observations and, subsequently, NuSTAR observations, which showed that the spectra of ULXs turn over around $\sim$5 keV (e.g., Stobbart et al. 2006; Bachetti et al. 2013; Sutton et al. 2013; Walton et al. 2014), demonstrating an "ultraluminous" spectral state (Gladstone et al. 2009) distinct from the canonical sub-Eddington accretion states, which exhibit power-law emission up to far higher photon energies (Remillard & McClintock 2006; Done et al. 2007).

The ultraluminous spectral state tends to exhibit two thermal components (Middleton et al. 2015a), as well as a steep power-law-like excess above $\sim$10 keV (e.g., Walton et al. 2018c). Typically, the hard thermal component can be fitted with a broadened disk model and may correspond to emission from the

central region of a super-Eddington slim disk in which advection plays a significant role, which has a broader temperature profile compared to a sub-Eddington thin disk (Abramowicz et al. 1988; Watarai et al. 2000). The soft thermal component is typically fitted with a standard disk-blackbody model though it likely originates from a massive outflowing wind driven by the radiation pressure (Poutanen et al. 2007; Urquhart & Soria 2016). The presence of such winds was confirmed by the detection of blueshifted absorption features in multiple ULXs, indicating wind velocities of $\sim$0.2c (Middleton et al. 2014, 2015b; Pinto et al. 2016, 2017; Kosec et al. 2018).

The detection of pulsations in a small number of ULXs (Bachetti et al. 2014; Fürst et al. 2016; Israel et al. 2017; Carpano et al. 2018; Rodríguez Castillo et al. 2019; Sathyaprakash et al. 2019) confirmed super-Eddington accretion in at least some of the ULX population since pulsations indicate the presence of a neutron star accretor, with the high luminosities indicating accretion happening at tens to hundreds of times the Eddington limit. The pulsed fraction of neutron star ULXs is found to increase with energy, with the pulsed spectrum having the cutoff power-law shape expected of an accretion column (Brightman et al. 2016; Walton et al. 2018b). This feature accounts for the steep power-law excess above 10 keV in these sources though this excess is also seen in sources from which pulsations have not yet been detected (Walton et al. 2018c). This may indicate that more of the ULX population has neutron star accretors than just those for which we detect pulsations or that magnetic and nonmagnetic sources are capable of producing similar spectra
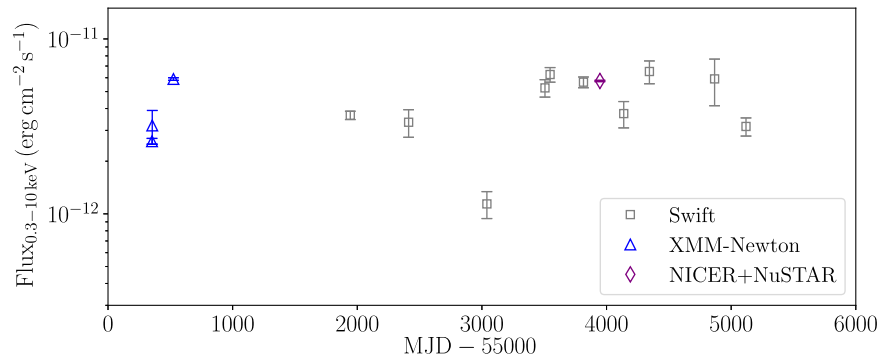
Figure 1. Long-term light curve of NGC 4190 ULX-1 in the 0.3–10 keV energy range. Swift-XRT observations are plotted with gray squares, XMM-Newton data with blue triangles, and NICER+NuSTAR data with purple diamonds. Swift fluxes are retrieved from the product generation tools provided on the Swift website; XMM-Newton and NICER+NuSTAR fluxes are retrieved from spectral fitting and converted to the 0.3–10 keV energy range where necessary (see Section 3).

and further details are required to distinguish them. Recent simulation work has demonstrated that a hard excess over a Wien tail can be produced by the inner regions of a super-Eddington accretion flow even in the absence of an accretion column (e.g., Mills et al. 2023).

In addition to pulsations, a number of other timing properties are observed in the ULX population. While much of the population of ULXs do not show strong short-term variability (e.g., Feng & Kaaret 2005), some do show significant stochastic variability rising to low frequencies (e.g., Heil et al. 2009). For some sources with sufficiently long observational coverage, there is a break at low frequencies (1–100 mHz) giving rise to flat-topped noise (e.g., Earnshaw et al. 2016), which is also seen in the Galactic supercritical source SS433 (Atapin et al. 2015). With some exceptions, the presence of strong variability appears to mainly correspond to sources with softer spectra, which has been proposed to be due to variability being imprinted on the hard central emission by a clumpy outflowing wind along the line of sight (e.g., Middleton et al. 2011, 2015a; Sutton et al. 2013). A small number of ULXs also show quasiperiodic oscillations (QPOs; e.g., Feng & Kaaret 2007; Rao et al. 2010; Agrawal & Nandi 2015), which may have the potential to provide insight into the geometry of the system.

The Neutron Star Interior Composition Explorer (NICER) telescope mounted on the International Space Station, with its large effective area and 100 ns timing resolution, is an excellent instrument for spectral and timing studies of X-ray binaries. However, since it is a nonfocusing instrument, its application to ULXs is limited due to the lower flux of extragalactic sources and the source confusion caused by multiple bright sources in a single galaxy. Nevertheless, it has successfully been used for the analysis of NGC 300 ULX-1 (Ray et al. 2019; Ng et al. 2022), which demonstrates its capacity for investigating bright and isolated ULXs.

NGC 4190 ULX-1 is a bright ULX in the nearby irregular galaxy NGC 4190 at ∼2.9 Mpc (Tully et al. 2016), located at $12^h 13^m 45{\overset{s}{.}}2 + 36° 37' 54''$ (Evans et al. 2019). The source is persistently bright but variable over time and has previously exhibited interesting spectral behavior, with an unusually low turnover energy in the XMM-Newton band of 2–4 keV (Ghosh & Rana 2021), potentially making its high-energy excess particularly accessible for study. It also demonstrates varying high-energy emission above the turnover, in contrast to some other ULXs for which the high-energy emission remains

remarkably consistent despite significant variability at lower energies (e.g., Walton et al. 2017, 2020).

While previously identified as a high-flux ULX ($3–7 \times 10^{-12}$ erg s^{-1} cm^{-2}) from XMM-Newton observations (Earnshaw et al. 2019), NGC 4190 ULX-1 was initially not followed up with instruments such as NuSTAR due to its proximity to the center of its host galaxy (∼10″), which in many cases means that the X-ray emission of a source will suffer from confusion from the galactic nucleus for instruments without the resolving power of Chandra. However, examination of an archival observation of NGC 4190 using the High Resolution Camera on Chandra shows that NGC 4190 ULX-1 is the only bright X-ray source in the galaxy and within the 5′ field of view of NICER (one other, far fainter source exists within 25″, too faint to contaminate a NICER spectrum). The existing Swift-XRT observations of the source (retrieved from the online light-curve generation facility on the Swift website; Evans et al. 2009) show it to demonstrate significant long-term variability (Figure 1).

Its isolation on the sky, combined with a relatively high flux from its proximity to us, make NGC 4190 ULX-1 an ideal ULX to be observed with NICER and NuSTAR in order to investigate its spectral and timing properties.

In this paper, we detail the analysis of a new simultaneous observation of NGC 4190 ULX-1 with NICER and NuSTAR, along with a reanalysis of archival XMM-Newton data in light of our discoveries. In Section 2 we describe the observations and data reduction, in Section 3 we describe the spectral and timing analysis, and in Section 4 we present our discussion and conclusions. We note that an independent paper on this source (Combi et al. 2024) was released while this work was under submission, and we provide some comparisons between these two works.

2. Data Reduction

On 2020 April 26, we performed a simultaneous observation of NGC 4190 with NICER (Observation ID: 3645010101–4) and NuSTAR (Observation ID: 30601009002) for total good exposure times of 24.7 ks and 85.0 ks, respectively, in order to investigate its broadband spectral and timing properties (PI: Earnshaw). There are also three archival observations of the galaxy taken with XMM-Newton in 2010, which we use to investigate its long-term spectral variability. We detail the observations used in this investigation in Table 1.

Table 1
The Observations Used in This Investigation, Consisting of Archival XMM-Newton Observations from 2010, and the NICER and NuSTAR Observations Taken for This Investigation

Observatory	Observation ID	Start Time	Exposure Time (ks)
XMM-Newton	0654650101	2010-06-06 12:08:27	6.2/6.2/0.2[a]
	0654650201	2010-06-08 11:14:45	15.2/16.9/5.9
	0654650301	2010-11-25 01:24:51	14.4/14.8/8.0
NICER	3645010101	2020-04-26 19:02:09	24.7[b]
	3645010102	2020-04-27 01:13:10	
	3645010103	2020-04-28 00:26:11	
	3645010104	2020-04-28 23:39:51	
NuSTAR	30601009002	2020-04-26 19:31:09	78.4 + 11.8[c]

Notes.
[a] XMM-Newton exposure times are given for the EPIC MOS1/MOS2/pn instruments after filtering for background flaring.
[b] NICER exposure time after combining and filtering all four observations.
[c] NuSTAR exposure time taken in mode 1 and mode 6, respectively.

2.1. NICER

The NICER data were reduced using NICERDAS version 2020-04-23_V007a, with CALDB version 20200722. Calibration and prefiltering were performed using the NICERL2 routine, and barycenter correction was applied with BARYCORR (with ephemeris DE-405), using the Chandra source coordinates (Evans et al. 2019). The four observations were then merged using NIMPUMERGE, and good time intervals (GTIs) were created using the following settings: SUN_ANGLE > 60, COR_SAX > 4.0, and KP < 5. These GTIs were used to extract events between 0.2 and 12 keV using NIEXTRACT-EVENTS, and then XSELECT was used to extract spectra and light curves. We used the standard response matrix file (RMF) and on-axis ancillary response file (ARF) as provided in the CALDB and generated the background spectrum using both the NICER_BKG_ESTIMATOR tool and the NIBACKGEN3C50 tool.

The count rate for NGC 4190 ULX-1 is comparable to the NICER background rate. Plotting the count spectrum along with the background shows that the background dominates over the data at low and high energies (Figure 2) though the two methods for background estimation do not entirely agree on the exact energy range for which the source is dominant. Therefore, we take an approximate average of the low- and high-energy bounds and only consider data in the energy range 0.5–4.5 keV when analyzing this source. Additionally, we used the background generated from the NICER_BKG_ESTIMATOR method during analysis as it is more conservative about the contribution from background than NIBACKGEN3C50. Using NICER_BKG_ESTIMATOR as a basis, we estimate the background count rate at 0.77 ct s^{-1} between 0.5 and 4.5 keV (compared to a net source rate of 1.75 ct s^{-1} in the same band).

2.2. NuSTAR

The NuSTAR data were reduced using NUSTARDAS V2.0.0, with CALDB version 20211020. The data were reduced using the NUPIPELINE routine, and data products were extracted using NUPRODUCTS with barycenter correction applied, using a 60$''$ radius source extraction region centered on the point-spread function defined for each of the FPMA and FPMB cameras. Background regions of 90$''$ radius located on the same chip were used to extract background products. The normal science mode (i.e., mode 1) contained 78.4 ks of good time data. A significant portion of the observation was spent in mode 6 (when aspect reconstruction using Camera Head Unit 4, CHU4, is unavailable), so we also used NUSPLITSC to produce event files for the alternate CHU combinations. Data products were then extracted from these additional event files and combined with the mode 1 products using the HEASoft tools LCMATH and ADDASCASPEC. For a more detailed description of the mode 6 data extraction process, see Walton et al. (2016). In this way, we were able to utilize 11.8 ks of additional data.

Plotting the combined count spectrum with the background shows the source data dominating over background up to 20 keV (Figure 2). Therefore, we limited the NuSTAR data to the range 3–20 keV for this analysis.
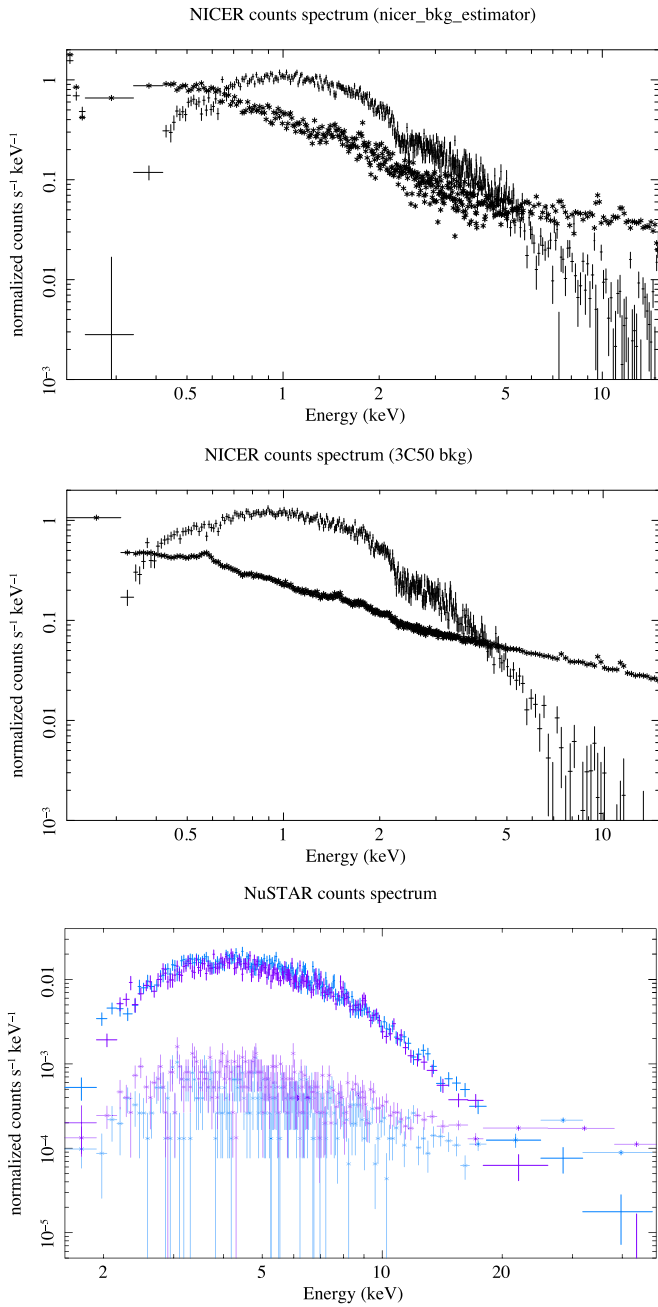
2.3. XMM-Newton

As well as the NICER and NuSTAR data from our observation, we also used XMM-Newton data from three archival observations of NGC 4190 ULX-1. We extracted and reduced EPIC-MOS and pn data using the XMM-Newton Science Analysis Software v17.0.0. The data were reduced using the EMPROC and EPPROC routines, and following standard procedures, we filtered for background flaring where the MOS count rate exceeded 0.35 ct s^{-1} in the 10–12 keV band and where the pn count rate exceeded 0.4 ct s^{-1} in the >12 keV band. Observation 0654650101 was particularly affected by flaring, and we do not use the pn data for this observation. Spectra and light curves in the 0.3–10 keV energy band were extracted from 40$''$ radius source regions, using FLAG == 0 and PATTERN < 4 events for the pn camera and PATTERN < 12 for the MOS cameras. Background products were extracted from 60$''$ regions on the same chips at a similar distance from the readout node. The RMF and ARF were generated using the RMFGEN and ARFGEN tasks.

3. Analysis and Results

NGC 4190 ULX-1 is persistently bright over the course of our observation, with an average NICER net count rate of 1.75 ct s^{-1} in the 0.5–4.5 keV energy range (compared with 0.77 ct s^{-1} due to background) and NuSTAR count rate of 0.3 ct s^{-1}. The source declines in flux slightly about halfway through the NICER observation, toward the end of the NuSTAR observation (Figure 3).

3.1. Spectral Analysis

We performed all spectral fitting using v12.10 of the XSPEC (Arnaud 1996) software, and all quoted models are given in XSPEC syntax. In all cases, spectra were grouped into at least 20 counts per bin to allow for χ^2 statistics to be used in fitting. Uncertainties are given at the 90% confidence level, and we use the abundance tables of Wilms et al. (2000) throughout. Where we use two tbabs absorption models, the first is always frozen to the Galactic value of $N_H = 1.84 \times 10^{20}$ cm^{-2} (Kalberla et al. 2005). We also use a constant const model, fixed to 1 for the NICER data, to account for calibration differences between the instruments. We give the parameters of all fits in Table 2.

NICER counts spectrum (nicer_bkg_estimator)

NICER counts spectrum (3C50 bkg)

NuSTAR counts spectrum

Figure 2. Count spectra including background for NICER (black) and NuSTAR FPMA and FPMB (blue and purple). The NICER background is plotted as estimated using NICER_BKG_ESTIMATOR (top) and NIBACKGEN3C50 (middle).

We fitted the NICER spectrum simultaneously with the NuSTAR FPMA and FPMB spectra. Since the broadband spectrum exhibits clear curvature, we began by fitting it with single-component absorbed-broadened-disk and cutoff power-law models, as sometimes observed in high-luminosity ULXs (e.g., Pintore et al. 2017; Sutton et al. 2017) and expected to be produced by a supercritical accretion disk or an accretion column, respectively. Neither model provided a good fit to the data ($\chi^2_\nu \sim 1.4$), and the residuals show an "m-shaped" structure that indicates spectral curvature not described by the model.

In order to fit this additional curvature, we next used an absorbed two-thermal-component model, `tbabs * tbabs *`

NGC 4190 ULX−1

Bin time: 200.0   s
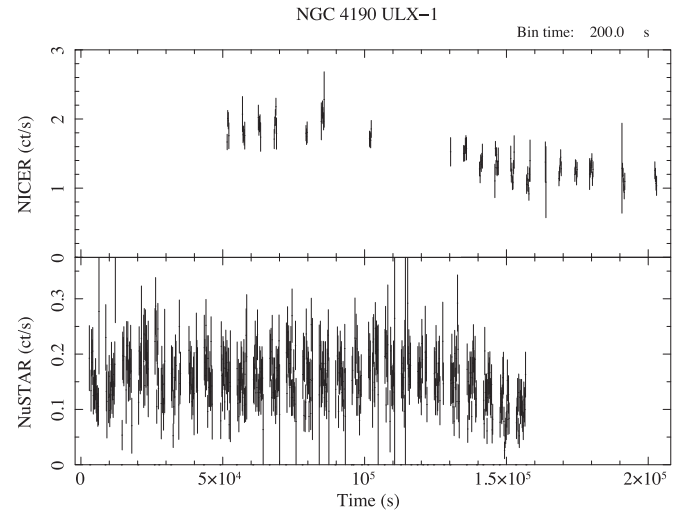
Figure 3. The light curve for NICER (0.5–4.5 keV) and NuSTAR (3–20 keV) over the course of the observation, in 200 s time bins. Both light curves are background subtracted (with the background assumed to be a constant $0.77 \, \mathrm{ct \, s^{-1}}$ for the NICER light curve).

(`diskbb+diskpbb`), often used to fit "ultraluminous state" ULX spectra, where the hotter broadened disk component is expected to be produced by an inner super-Eddington slim disk and the cooler disk component originates from a massive outflowing wind or potentially an outer sub-Eddington thin disk in the case of an intermediate-mass black hole. This offers an improvement on the singular `diskpbb` model, but there is still an obvious excess at energies above 10 keV, as commonly seen in broadband observations of ULXs (e.g., Walton et al. 2014, 2015; Mukherjee et al. 2015; Figure 4, top).

To account for the excess high-energy emission, we followed the approach of Walton et al. (2020) and fitted the spectra with both a magnetic model and a nonmagnetic model. The magnetic model, `tbabs * tbabs * (diskbb +diskpbb+cutoffpl)`, assumes the high-energy emission to originate from an accretion column onto a neutron star with a strong magnetic field. Since we do not detect pulsations from this source (see Section 3.2) and are therefore unable to isolate a pulsed spectrum, we assume typical ULX pulsar parameters $\Gamma = 0.5$ and $E_{\mathrm{cut}} = 8.1$ keV for the cutoff power-law component as in Walton et al. (2018c). For the nonmagnetic model, `tbabs * tbabs * (diskbb+simpl * diskpbb)`, we assume that the high-energy excess originates instead from Compton upscattering of disk photons close to the accretor, and so we model the component with the `simpl` convolution model (Steiner et al. 2009) applied to the hotter `diskpbb` component.

We find that both the magnetic and nonmagnetic models provide similarly good fits to the data, with no further components evident in the residuals. Interestingly, when a high-energy component is added to the model, the `diskpbb` component is no longer required to be broadened, with the radial dependence of the disk temperature p tending toward high values and consistent in each case with a value of ≈ 0.75 and therefore equivalent to a standard `diskbb` model. We therefore also fitted the spectra with models that replace the `diskpbb` components with a second `diskbb` component instead and find similarly good fits (Figure 4, middle and bottom). Using the `cflux` convolution model, we calculated

Table 2
The Parameters of All Multicomponent Spectral Fits to the Joint NICER and NuSTAR Observation of NGC 4190 ULX-1, as well as for Archival XMM-Newton Observations

Model tb * tb * (...)	$N_{\rm H}$[a] ($\times 10^{21}$ cm^{-2})	$T_{\rm in,1}$ (keV)	norm$_1$	$T_{\rm in,2}$ (keV)	p	norm$_2$ ($\times 10^{-3}$)	Γ	$f_{\rm scat}/E_{\rm cut}$ .../(keV)	norm$_3$ ($\times 10^{-5}$)	c[b]	χ^2/dof
				NICER 3645010101–4 + NuSTAR 30601009002							
dbb+dpbb	3.9 ± 0.7	0.15 ± 0.02	400^{+740}_{-290}	2.50 ± 0.09	0.60 ± 0.02	$4.2^{+1.1}_{-0.9}$	...	...	...	1.05 ± 0.04	1078.5/767
dbb+s * dpbb	$2.4^{+0.4}_{-0.3}$	$0.28^{+0.04}_{-0.05}$	14^{+19}_{-7}	$1.2^{+0.3}_{-0.1}$	>0.76	210^{+80}_{-150}	$3.0^{+0.2}_{-0.3}$	0.5 ± 0.2	...	$1.23^{+0.06}_{-0.05}$	964.7/765
dbb+dpbb+cpl	$2.5^{+0.6}_{-0.5}$	$0.25^{+0.06}_{-0.05}$	19^{+43}_{-12}	1.6 ± 0.1	$0.76^{+0.15}_{-0.08}$	40^{+30}_{-10}	0.5	8.1	7.1 ± 0.7	1.09 ± 0.04	962.9/766
dbb+s * dbb	$2.7^{+0.5}_{-0.4}$	$0.23^{+0.03}_{-0.02}$	28^{+33}_{-16}	1.5 ± 0.1	...	60^{+20}_{-10}	$2.7^{+0.4}_{-0.5}$	$0.3^{+0.2}_{-0.1}$	...	$1.23^{+0.07}_{-0.06}$	967.9/766
dbb+dbb+cpl	2.6 ± 0.4	$0.25^{+0.03}_{-0.02}$	21^{+20}_{-11}	1.61 ± 0.06	...	37^{+5}_{-4}	0.5	8.1	7.0 ± 0.6	1.09 ± 0.04	962.9/767
dbb+dbb+cpl[c]	2.6 ± 0.4	0.24 ± 0.03	26^{+27}_{-14}	1.5 ± 0.1	...	43^{+10}_{-9}	0.4 ± 0.5	6^{+4}_{-2}	$9.6^{+1.1}_{-0.6}$	1.09 ± 0.04	965.0/776
dbb+dpbb+cpl[c]	$2.3^{+0.5}_{-0.3}$	0.29 ± 0.05	12^{+21}_{-3}	$1.4^{+0.2}_{-0.1}$	>0.75	110^{+30}_{-70}	$0.3^{+0.4}_{-0.7}$	5^{+3}_{-1}	12^{+16}_{-8}	1.09 ± 0.04	962.4/775
				XMM-Newton 0654650101							
dbb+s * dbb	1.0	$0.20^{+0.09}_{-0.07}$	11^{+65}_{-9}	$1.10^{+0.09}_{-0.08}$	...	80 ± 20	2.7	0.3	...	...	99.2/95
dbb+dbb+cpl	1.0	$0.21^{+0.09}_{-0.07}$	10^{+50}_{-8}	$1.21^{+0.09}_{-0.08}$	...	50^{+20}_{-10}	0.5	8.1	2.4	...	97.5/95
				XMM-Newton 0654650201							
dbb+s * dbb	$1.5^{+0.6}_{-0.5}$	$0.22^{+0.07}_{-0.04}$	14^{+38}_{-11}	1.11 ± 0.05	...	90 ± 20	2.7	0.3	...	...	252.1/246
dbb+dbb+cpl	$1.5^{+0.6}_{-0.5}$	$0.23^{+0.07}_{-0.04}$	12^{+35}_{-10}	1.20 ± 0.05	...	60 ± 10	0.5	8.1	3.7	...	251.8/246
				XMM-Newton 0654650301							
dbb+s * dbb	0.8 ± 0.6	$0.5^{+0.2}_{-0.1}$	$0.8^{+2.1}_{-0.5}$	$1.6^{+0.2}_{-0.1}$	...	40 ± 10	2.7	0.3	...	...	304.7/309
dbb+dbb+cpl	$0.8^{+0.3}_{-0.2}$	$0.4^{+0.2}_{-0.1}$	$0.9^{+2.4}_{-0.6}$	1.6 ± 0.1	...	30 ± 10	0.5	8.1	7.5	...	304.9/309

Notes. Where no uncertainties are given, parameters are frozen. XSPEC model abbreviations: tb = tabs, cpl = cutoffpl, dbb = diskbb, dpbb = diskpbb, s = simpl.

[a] $N_{\rm H}$ for the second tbabs component; the first is frozen to the Galactic value of $N_{\rm H} = 1.84 \times 10^{20}$ cm^{-2}.

[b] Normalization constant between NICER and NuSTAR.

[c] Cut-off power-law parameters found by fitting simultaneously with the covariance spectrum.
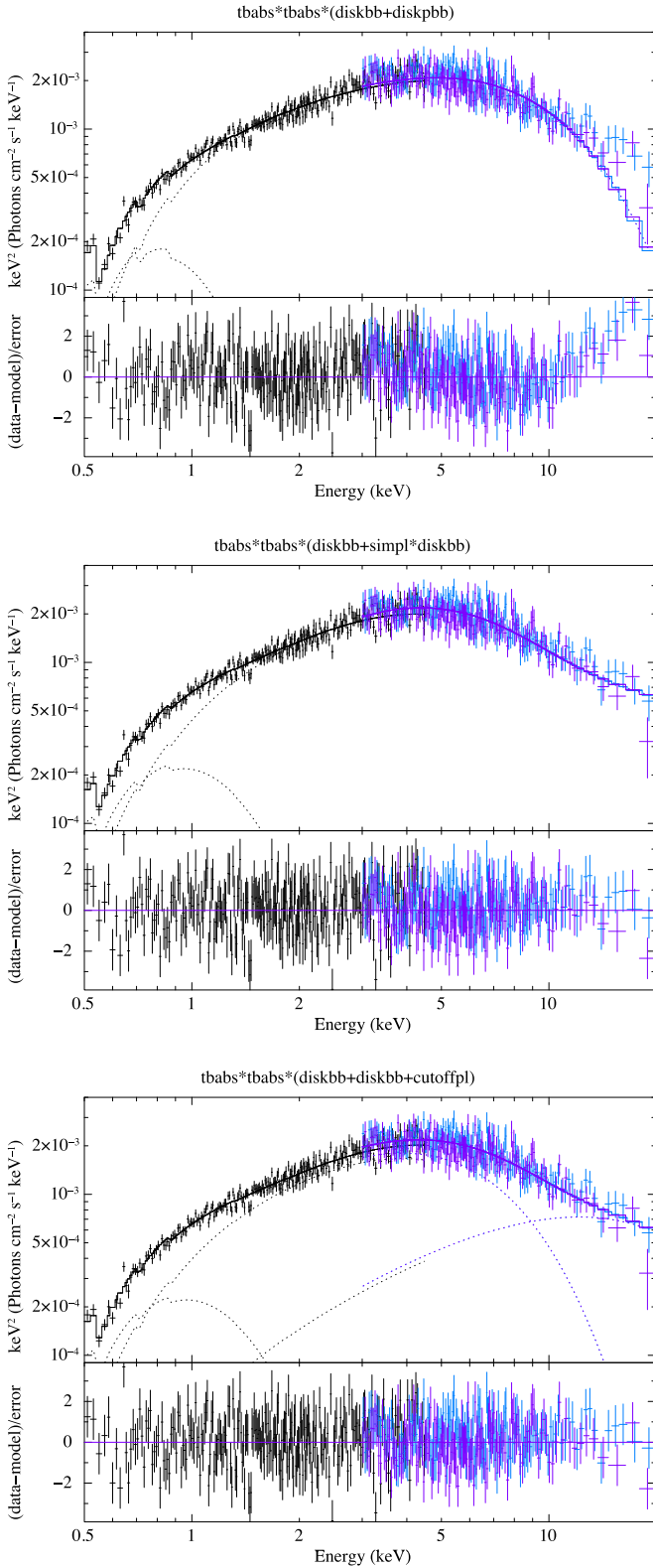
Figure 4. The unfolded spectrum and residuals for three of the models used to fit the joint NICER (black) and NuSTAR (blue and purple) data. Spectra rebinned for visual clarity. Top: `tbabs * tbabs * (diskbb+diskpbb)`. A high-energy excess is evident in the residuals. Middle: `tbabs * tbabs * (diskbb+simpl * diskbb)`. Bottom: `tbabs * tbabs * (diskbb +diskbb+cutoffpl)`.

the 0.3–10 keV flux to be $5.8 \pm 0.5 \times 10^{-12} \, \mathrm{erg \, s^{-1} \, cm^{-2}}$, equivalent to a luminosity of $5.8 \times 10^{39} \, \mathrm{erg \, s^{-1}}$ at 2.9 Mpc. This is the value for the `tbabs * tbabs * (diskbb`
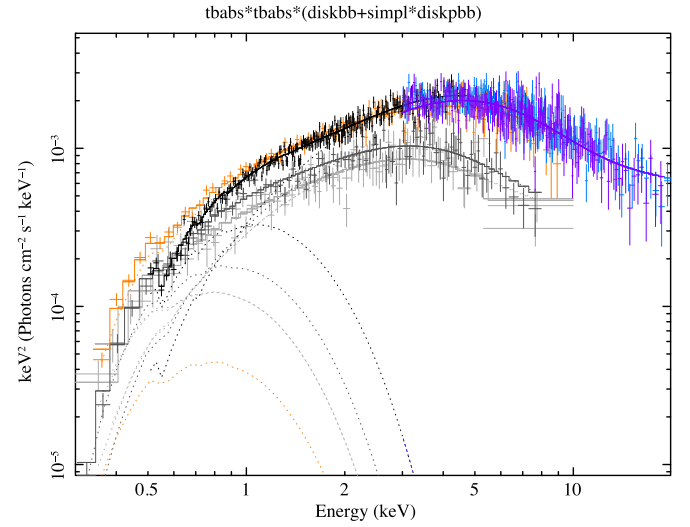

Figure 5. The unfolded spectra for the three archival XMM-Newton observations (0654650101 in light gray, 0654650102 in dark gray, 0654650103 in orange), plotted alongside the NICER and NuSTAR spectra (colors as in Figure 4).

`+diskbb+cutoffpl)` model though the other models incorporating the high-energy excess all give similar fluxes.

While the archival XMM-Newton data can be acceptably fitted with single-component models (Ghosh & Rana 2021), we assume that the underlying source spectrum is similar to what we observe for the joint NICER and NuSTAR observation. Therefore we fit the XMM-Newton observations with the magnetic and nonmagnetic models (using two `diskbb` components to reduce the number of free parameters) in order to trace how the different spectral components change between observations. Since there is no high-energy coverage for these observations, we freeze the parameters of the `simpl` component to $\Gamma = 2.7$ and $f_{\mathrm{scat}} = 0.3$ as in the best-fitting model using two `diskbb` components for the broadband data set and freeze the normalization of the `cutoffpl` component to the upper limit found on an initial unfrozen fit so that its presence in the model will have a similar impact on the parameters of the hot thermal component as in the broadband fit. We also freeze the second `tbabs` component to $1 \times 10^{21} \, \mathrm{cm^{-2}}$ for the first XMM-Newton observation (based on the fits to the other two XMM-Newton observations) since there is insufficient low-energy data to achieve good constraints due to the low good exposure time.

We find that there is no significant difference between the parameters for the thermal components in the magnetic model compared with the nonmagnetic model. In both cases, the first two lower-flux observations show lower temperatures in both thermal components than the third observation, which is closer in flux to the broadband epoch. However, the cool thermal component is very similar in temperature between the lower-flux XMM-Newton observations and the broadband observation, showing a slight increase in temperature for the third XMM-Newton epoch (this may be degenerate with a decrease in N_{H}, which we also see for this observation). The hot component temperature is very similar between the third XMM-Newton epoch and the broadband spectrum. We plot the XMM-Newton spectra alongside the broadband NICER+NuSTAR spectrum in Figure 5.

We did attempt to split the data by time based on the slight decrease in flux during the course of the observation (see
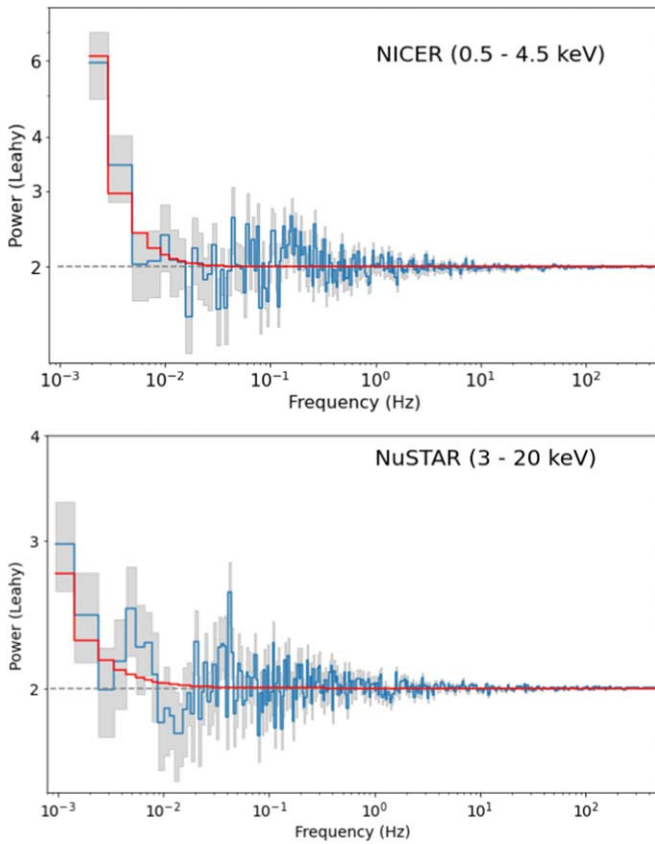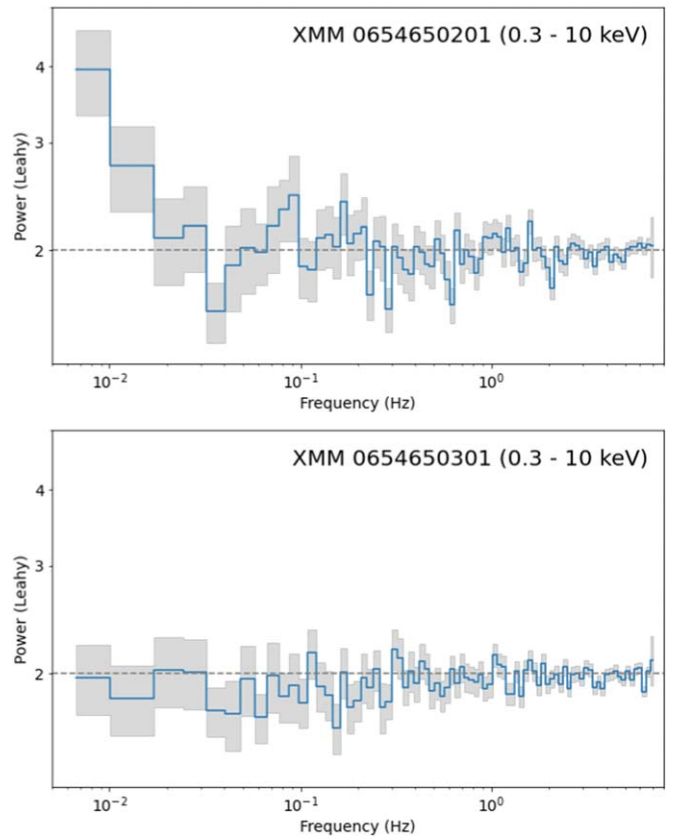
Figure 6. The power spectra for NICER (top) and NuSTAR (bottom) in Leahy normalization, with errors given in gray filled regions, the Poisson noise level indicated with a dashed gray line, and the best-fitting power-law models plotted in red.


Figure 7. The power spectra for the XMM-Newton observations 0654650201 (top) and 0654650301 (bottom) in Leahy normalization, with errors given in gray filled regions and the Poisson noise level indicated with a dashed gray line.

Figure 3) although we were not able to find any significant differences in model parameters on this basis.

3.2. Timing Analysis

We generated power spectra using v1.0 of the `stingray` python package for X-ray timing (Bachetti et al. 2022). For the NICER observation, we binned the source events within the 0.5–4.5 keV energy range into a light curve with $dt = 0.001$ s and broke the light curve into segments of length 524.288 s ($2^{19} \times dt$). This generated 42 segments, which we used to create an average power spectrum with approximately Gaussian uncertainties, allowing for fitting using χ^2 statistics. The spectrum was geometrically rebinned by a factor of 1.03 and normalized using Leahy normalization (where the Poisson white-noise level is set to 2). We followed a similar process for the NuSTAR power spectrum, using the combined FPMA and FPMB events within 3–20 keV, binning the light curve with $dt = 0.001$ s and creating an average power spectrum using 67 segments of length 1048.576 s ($2^{20} \times dt$), binned and normalized in the same fashion. Both power spectra were converted to XSPEC format using the `flx2xsp` FTOOL so that they could be fitted using the XSPEC software (see Appendix A1 of Ingram & Done 2012).

Both power spectra are mostly featureless except for stochastic noise increasing toward lower frequencies below ∼0.01 Hz (Figure 6). Using the Whittle statistic (Whittle 1953), and accounting for the Poisson noise using a flat power-law with normalization set to 2, both can be fitted with a power law

$P(f) \propto f^{-\alpha}$ with $\alpha \approx 1$–2, as expected for red noise often seen in accretion processes and seen in some of the ULX population (Heil et al. 2009). For NICER, we find $\alpha = 2.10^{+1.9}_{-0.6}$; for NuSTAR, we are unable to obtain strong constraints and simply find $\alpha > 0.8$. Neither power spectrum shows any evidence of the presence of a QPO. The fractional rms below 0.1 Hz is ∼0.06 for NICER and ∼0.18 for NuSTAR. In other words, there is a higher contribution to the variability in the NuSTAR band although there is better signal-to-noise in the NICER band.

We performed a similar analysis for the two archival XMM-Newton observations with a significant amount of usable EPIC-pn data (the first observation suffered from large amounts of background flaring and only had 200 s of good EPIC-pn time), using $dt = 0.0734$ s (i.e., the time resolution of the EPIC-pn camera) and segments of length 150.3232 s ($2^{11} \times dt$), for 39 and 58 segments for observations 0654650201 and 0654650301, respectively (Figure 7). For 0654650201, we see similar stochastic variability toward low frequencies with $\alpha \approx 2$ (although similar to the NuSTAR power spectrum, we are unable to place strong constraints on the slope), and the fractional rms below 0.1 Hz is approximately ∼0.17. However, for 0654650301, we do not see any significant variability above the Poisson noise level.

While there are no obvious pulsation signals in the power spectra, processes such as spin-up or orbital modulation often mean that genuine pulsations do not show up in a straightforward power spectrum. Therefore, we ran an accelerated

tbabs*tbabs*(diskbb+diskbb+cutoffpl)
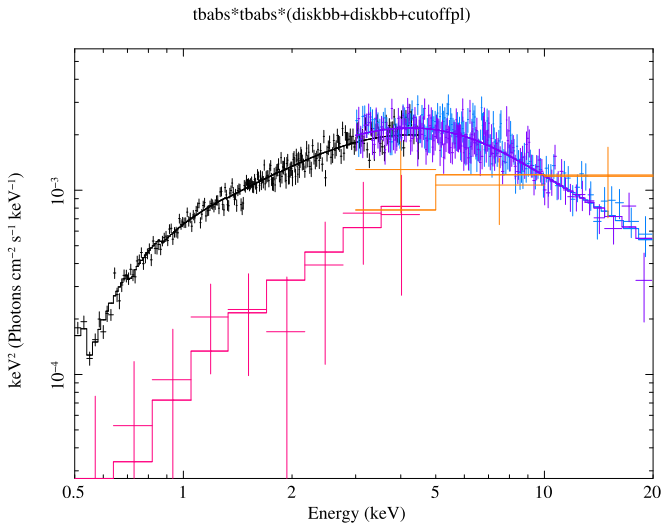
Figure 8. The NICER and NuSTAR energy spectrum (colors as in Figure 4), plotted with the covariance spectrum (magenta and orange for NICER and NuSTAR, respectively).

pulsation search on the NICER, NuSTAR, and the latter two XMM-Newton observations using the HENaccelsearch routine from v7.0 of the HENDRICS timing software (Bachetti 2018), searching for pulsations between 0.01 and 10 Hz with acceleration between 10^{-10} and 5×10^{-9} Hz s^{-1}. We did not find any significant signals in any of the observations using this method.

The reasonably high number of photons from the NICER and NuSTAR observations allows us to place relatively constraining upper limits on the pulsed fraction. To estimate an upper limit on the pulsed fraction, we used stingray to simulate light curves matching the GTIs and average count rate of both observations, with the addition of a sinusoidal pulsation signal at a period of 1 s fairly typical of ULX pulsars (e.g., Bachetti et al. 2014; Israel et al. 2017; Sathyaprakash et al. 2019) at a variety of pulsed fractions. We simulated 100 light curves for each pulsed fraction in the range $10\% < \mathrm{PF} < 50\%$ in steps of 0.5% and searched for pulsations using epoch folding (we did not simulate any kind of acceleration as this ultimately has no effect on the upper limit and allows us to use a more straightforward pulsation search). We define the upper limit as the pulsed fraction for which at least 90% of simulations detected the pulsation with a significance of at least 3σ. We find an upper limit on the pulsed fraction of 16% for NICER (0.5–4.5 keV) and 35% for NuSTAR (3–20 keV).

To further explore the variability of NGC 4190 ULX-1, we computed the covariance spectrum (Wilkinson & Uttley 2009), shown in Figure 8. The covariance spectrum shows correlated variability as a function of energy, which may allow us to identify the spectral components that are the source of coherent variability, and has previously been used to disambiguate the multiple components of the energy spectra of ULXs (Middleton et al. 2015a, 2019; Kara et al. 2020). We find that the covariance increases toward higher energies although it does not appear to directly match the spectral shape of the hot thermal component—if fitted with a diskbb or diskpbb model, we find that it requires temperatures of $T_{\rm in} > 3$ keV, far higher than that found for $T_{\rm in,2}$, regardless of the model used to fit the spectrum. The covariance spectrum does, however, appear to resemble the cutoff power-law component used to model a potential accretion column in the magnetic model

although by itself it cannot constrain a cutoff energy, so we proceeded to fit it simultaneously with the broadband energy spectrum, including an additional normalization constant to account for the lower normalization expected for the covariance spectrum, and tying the parameters of the cutoffpl component to those fitted to the covariance spectrum.

We find that, with the cutoffpl parameters so constrained, the lower-energy portion of the spectrum still requires two thermal components to be fitted well. Attempting to fit the spectrum with the high-energy cutoff power law and a single softer thermal component (whether broadened or not) or with a diskbb+nthcomp model similar to that used by Middleton et al. (2015a), results in a poorer fit ($\chi^2 > 1000$ in each case) and the "m-shaped" residuals in the NICER data indicating the presence of two components. Therefore, using the tbabs * tbabs * (diskbb+diskbb+cutoffpl) model, we find the cutoff power-law parameters $\Gamma = 0.4 \pm 0.5$ and $E_{\rm cut} = 6^{+4}_{-2}$ keV very similar to those earlier assumed to be representative of a ULX pulsar accretion column. The parameters for the thermal components were also found to be similar to the previous broadband spectral fit. We also tried fitting the hotter of the two thermal components with a diskpbb model to see whether there is any evidence of broadening when the cutoff power-law parameters are constrained by the covariance spectrum. In this case as well as before, the radial temperature dependence p tends toward the maximal value of 1 (indicating a narrower spectral component) with a lower limit of $p > 0.75$, ruling out a spectrally broadened disk component.

4. Discussion

NGC 4190 ULX-1 has a spectrum typical of the overall ULX population, with two thermal components below 10 keV and an additional hard excess. Its spectrum is generally hard, with the hotter thermal component the dominant of the two, and there are no significant residuals around 1 keV as found in some ULXs more dominated by soft emission (Middleton et al. 2014, 2015b), which are indicative of powerful, relativistic outflowing winds (Pinto et al. 2016). This suggests that we are viewing the source at a relatively low inclination, with most of the emission originating from accretion at the center of the system. There is a clear high-energy excess above 10 keV although we cannot determine whether the origin of this component is magnetic or nonmagnetic from the spectrum alone, as both models provide fits of similar quality. The particularly low-energy turnover for a ULX appears to result from the hot thermal component not showing the broadening typically exhibited in ULX spectra, with values of p consistent with or higher than the standard thin-disk value of $p = 0.75$.

Similar to other ULXs that show significant stochastic variability (which is not a universal feature of ULXs, found in less than half of the population; Heil et al. 2009), NGC 4190 ULX-1 demonstrates red noise below 0.1 Hz in multiple observations. Many of the ULXs found to have high levels of variability have soft spectra (e.g., Sutton et al. 2013) though the covariance spectra of such sources (Middleton et al. 2015a) indicate that the variability is associated with the hotter thermal component, suggesting a model in which variability is imprinted upon the hard emission by a clumpy outflowing wind along the line of sight (Middleton et al. 2011; Takeuchi et al. 2013).

In contrast to these soft variable ULXs, NGC 4190 ULX-1 has a hard spectrum, and the covariance spectrum shows that its variability is not associated with the hot thermal component but is associated with the harder excess emission and appears to confirm its cutoff power-law nature. NGC 4190 ULX-1 is not unique in being a hard variable ULX—for example, M51 ULX-7 also has a hard spectrum and significant short-term variability, showing flicker noise as well as a low-frequency break in its power spectrum below 10^{-3} Hz (Earnshaw et al. 2016), and was later found to be a ULX pulsar (Rodríguez Castillo et al. 2019). Another example in the same galaxy is M51 ULX-8, a reasonably hard and variable source that is not a pulsating ULX but still proposed to be a neutron star accretor from the detection of a potential cyclotron absorption line in its spectrum (Brightman et al. 2018) and whose covariance spectrum shows that its variability also originates in a hard cutoff power-law component consistent with an accretion column and possibly resulting from a combination of accretion-column and inner-disk emission (Middleton et al. 2019).

The covariance spectrum of NGC 4190 ULX-1 suggests that the variability in this source originates not from its hot thermal component but from a cutoff power-law component with parameters similar to those typically found in ULX pulsars (e.g., Walton et al. 2018c). Therefore, despite the lack of detected pulsations, the timing properties of NGC 4190 ULX-1 nevertheless potentially provide indirect evidence of the presence of an accretion-column component. It is possible for a high-energy power-law excess to be generated by an accreting black hole ULX in the absence of an accretion column (e.g., Mills et al. 2023), and indeed Combi et al. (2024) find the spectral energy distribution of NGC 4190 ULX-1 to be consistent with a model that assumes a $10 M_\odot$ black hole accreting at $10 \dot{M}_{\mathrm{Edd}}$, but in this case, it is not clear whether the covariance spectrum would take the cutoff power-law form that we see here. If the accretor is indeed a neutron star with an accretion column, it is possible that the magnetic field and spin alignment of the neutron star are not favorable to produce pulsations.

We also note that the lack of detected pulsations do not rule out the presence of pulsations altogether. While we can rule out extremely high pulsed fractions such as the pulsed fraction of 72% found for NGC 300 ULX-1 in the NuSTAR band (Carpano et al. 2018) compared with our upper limit of 35% for NGC 4190 ULX-1 in the same band, several ULX pulsars have lower pulsed fractions than this even where they peak in the NuSTAR band. For example, pulsations of NGC 7793 P13 have been found to peak in the NuSTAR band at pulsed fractions of $\sim$20%–60% at different times (Fürst et al. 2016, 2021), and in the XMM-Newton band pulsations have been detected at pulsed fractions as low as a few percent (e.g., in NGC 1313 X-2; Sathyaprakash et al. 2019), lower than our NICER upper limit of 16%. Additionally, pulsed fractions lower even than this may well be present in the ULX population and simply be undetected due to the lack of sufficient data to detect them, given that detecting pulsations can be challenging anyway due to spin-up and orbital effects. (We note that Combi et al. 2024, following a different method, found pulsed fraction upper limits of 7% and 18% for NICER and NuSTAR, respectively, at the 90% significance level, which are approximately equivalent to our 3σ upper limits.)

The matter is further complicated by the fact that pulsations in ULX pulsars are sometimes found to be transient (e.g., Bachetti et al. 2020), such that multiple high-quality observations may be required to successfully identify a genuine ULX pulsar. Future observations with NuSTAR in particular, with a moderate (50%–100%) increase in exposure time, would be able to probe pulsed fractions down to 30% at energies above 10 keV (the energy range in which they are strongest in ULX pulsars), as well as provide more opportunities to search for transient pulsations.

Given the low frequency of the aperiodic variability we detect, it is unlikely to be intrinsic to an accretion column, which has a much shorter characteristic timescale than these observations are sensitive to, and variability is at any rate expected to be suppressed within the magnetospheric radius (Revnivtsev et al. 2009; Mushtukov et al. 2019). Instead, the variability could be imprinted upon the high-energy emission by a clumpy obscuring wind as described in Middleton et al. (2015a). This is in tension with the apparent low inclination of this source we mention at the beginning of this section, but given that the presence of a soft thermal component is evident, the inclination may be high enough for a small amount of the outflowing wind to intercept the line of sight to the center of the system and to make a modest contribution to the energy spectrum. At a favorable inclination, it may also be possible for most of the hot thermal emission from the super-Eddington disk to remain unobscured, leading to the component not making a significant contribution to the covariance spectrum.

The disappearance of short-term variability in the third XMM-Newton observation appears to be connected with an increase in the temperature of the soft thermal component and/or a decrease in the N_{H} of the absorption. In the case that the variability originates from the high-energy emission being partially obscured by a clumpy wind, this may indicate a decrease in the spherization radius R_{sph} due to a lowered mass accretion rate, leading to the clumpy wind no longer crossing the line of sight to the observer. The lack of high-energy data during the third XMM-Newton observation makes it difficult to determine the true contribution of a cutoff power-law component—while its normalization upper limit is consistent with what we measure for the broadband observation, we cannot confirm its presence from the XMM-Newton data alone, and it is possible that the high-energy component is itself absent in this observation. Further broadband observations of the source in multiple flux states would provide further insight into the behavior of the hard emission over time.

The long-term variability in the spectrum appears to be driven primarily by the temperature and flux of the hot thermal component rather than the cool component. Also, while we only have NuSTAR data for one of the epochs, the low-energy spectral turnover makes it clear that this ULX does not have a very stable high-energy tail (unlike that seen in some ULXs such as Ho IX X-1 and NGC 1313 X-1, which show considerable soft variability yet very consistent high-energy tails; Walton et al. 2017, 2020). For a nonmagnetic model in which the high-energy emission originates from upscattering of photons from the hot thermal component, this variability arises naturally from the changes in disk temperature changing the intrinsic spectrum that is upscattered. For the magnetic model, it implies a change in the flux of the accretion-column component, potentially due to a changing accretion-column height resulting from changes in the mass accretion rate through the column or changing obscuration of the accretion column.

We can explore the spectral variability further by making luminosity–temperature plots for the two thermal components (Figure 9). The XSPEC model `cflux` evaluated between 0.001
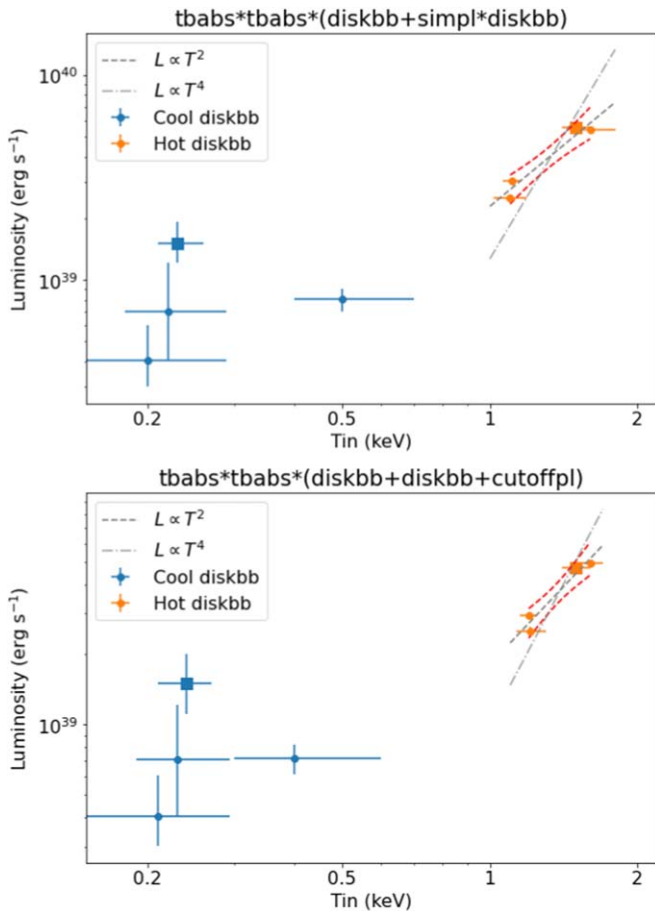
Figure 9. Unabsorbed luminosity–temperature relations for NGC 4190 ULX-1 when fitted with the nonmagnetic (top) and magnetic (bottom) models. The cool thermal component is plotted in blue, and the hot component is plotted in orange. The more reliable values obtained from the broadband observation are indicated with squares. The dark gray and red dashed lines indicate the line of best fit to the hot component and its errors, respectively, with a $L \propto T^4$ relation plotted with a lighter gray dotted–dashed line for comparison.

and 100 keV was used to estimate the unabsorbed bolometric luminosity for the two `diskbb` components in the `diskbb`-only fits (these chosen to reduce the number of free parameters). The constraints placed using the covariance spectrum fit were considered in the case of the broadband NICER and NuSTAR observation. No obvious trend is seen for the cool thermal component save for the higher-temperature observation appearing to be a distinct outlier. We note that the luminosities seen for this component are super-Eddington or nearly so, particularly in the case of a neutron star accretor, which suggests that this component results from a soft outflowing wind, ruling out a thin, sub-Eddington outer-accretion disk for this source.

In contrast, the hot thermal component appears to demonstrate a clear relationship between luminosity and temperature, which we found to be $L \propto T^{2.0 \pm 0.9}$ via least-squares fitting for the nonmagnetic model and similarly $L \propto T^{2.2 \pm 1.1}$ for the magnetic model. This result comes with obvious caveats—namely that the XMM-Newton spectra are overfitted by three-component models and are unable to constrain any of the high-energy component parameters; therefore, the uncertainties are underestimated and some parameters are potentially biased due to others being frozen. We are also working with a small number of observations clustered together in the L–T space, insufficient to make strong claims about the behavior over a wide range of luminosities

and disk temperatures. A higher number of truly broadband observations would be required to confirm this relationship.

However, if we take the relation at face value, it is interesting to note that despite there being no evidence for the spectral broadening expected from a slim, super-Eddington accretion disk, the L–T relation is more similar to the shallow $L \propto T^2$ relation expected for a slim disk (Watarai et al. 2000) compared with the $L \propto T^4$ expected for a standard sub-Eddington accretion disk (Shakura & Sunyaev 1973), implying that a slim disk may still be present (Combi et al. 2024 also favor a shallow $L \propto T^2$ relation over a $L \propto T^4$ relation in their analysis). It is possible that such a spectrally narrow thermal component could originate from a slim disk if it extends only over a small number of radii. We would normally expect a slim disk to reach all the way to the innermost stable circular orbit (ISCO) at the high mass accretion rates that would produce it, but the presence of a strong enough magnetic field from a neutron star accretor may truncate the disk before it reaches the ISCO (as suggested by Walton et al. 2018b), which would result in a narrower range of temperatures and an artificially high value of p when fitting with a `diskpbb` model. Therefore, if present, this shallow L–T relation combined with a narrow hot component may be tentative further evidence of the presence of a neutron star accretor, with a magnetospheric radius close to but slightly less than the spherization radius of the super-Eddington accretion disk. Ultimately, further broadband data are required to confirm this behavior.

5. Conclusions

We present the spectral and timing analysis of a broadband NICER+NuSTAR observation of the nearby and relatively understudied NGC 4190 ULX-1, which exhibits spectral features typical of the wider ULX population and significant spectral variability. While pulsations were not detected, the presence of a hard cutoff power-law component in the covariance spectrum and the luminosity–temperature properties of the narrow hot thermal component provide tentative evidence toward a neutron star accretor with an accretion column and a super-Eddington accretion disk truncated by the neutron star magnetic field.

The compelling possibility of NGC 4190 ULX-1 hosting a neutron star accretor, coupled with its nearby and highly accessible nature, make it an ideal target for future ULX study. Further broadband observations will be critical in confirming the luminosity–temperature trends suggested by the archival XMM-Newton observations for investigating the connection between the changing spectral and timing properties of this source and for further exploring the nature and behavior of its high-energy emission. Future observations will also be necessary to continue the search for pulsations in the case that they are simply transient in this source or other properties such as cyclotron lines that may be able to confirm the neutron star nature of this source (Brightman et al. 2018; Walton et al. 2018a).

While NICER is not typically used for ULX studies due to their comparatively low fluxes compared with the NICER background and their extragalactic nature making source confusion more likely, it is clear that it can still be a powerful tool for the timing analysis of the few ULXs that are nearby and reasonably well isolated. However, a full picture of the X-ray behavior of this source can only be obtained with broadband X-ray data. While coordination of a soft X-ray observatory with NuSTAR is invaluable with present-day

capabilities, this source illustrates the value of a future dedicated broadband observatory such as the High Energy X-ray Probe in the study of ULXs (Bachetti et al. 2023; Madsen et al. 2023).

ORCID iDs

Hannah P. Earnshaw ⓘ https://orcid.org/0000-0001-5857-5622
Matteo Bachetti ⓘ https://orcid.org/0000-0002-4576-9337
Murray Brightman ⓘ https://orcid.org/0000-0002-8147-2602
Felix Fürst ⓘ https://orcid.org/0000-0003-0388-0560
Fiona A. Harrison ⓘ https://orcid.org/0000-0002-4226-8959
Matthew Middleton ⓘ https://orcid.org/0000-0002-8183-2970
Renee Ludlam ⓘ https://orcid.org/0000-0002-8961-939X
Sean N. Pike ⓘ https://orcid.org/0000-0002-8403-0041
Daniel Stern ⓘ https://orcid.org/0000-0003-2686-9241
Dominic J. Walton ⓘ https://orcid.org/0000-0001-5819-3552

References

Abramowicz, M. A., Czerny, B., Lasota, J. P., & Szuszkiewicz, E. 1988, ApJ, 332, 646
Agrawal, V. K., & Nandi, A. 2015, MNRAS, 446, 3926
Arnaud, K. A. 1996, in ASP Conf. Ser. 101, Astronomical Data Analysis Software and Systems V, ed. G. H. Jacoby & J. Barnes (San Francisco, CA: ASP), 17
Astropy Collaboration, Price-Whelan, A. M., Sipőcz, B. M., et al. 2018, AJ, 156, 123
Astropy Collaboration, Robitaille, T. P., Tollerud, E. J., et al. 2013, A&A, 558, A33
Atapin, K., Fabrika, S., Medvedev, A., & Vinokurov, A. 2015, MNRAS, 446, 893
Bachetti, M. 2018, HENDRICS: High ENergy Data Reduction Interface from the Command Shell, Astrophysics Source Code Library, ascl:1805.019
Bachetti, M., Harrison, F. A., Walton, D. J., et al. 2014, Natur, 514, 202
Bachetti, M., Huppenkothen, D., Khan, U., et al. 2022, StingraySoftware/stingray: Version 1.0, Zenodo, doi:10.5281/zenodo.6394742
Bachetti, M., Maccarone, T. J., Brightman, M., et al. 2020, ApJ, 891, 44
Bachetti, M., Middleton, M. J., Pinto, C., et al. 2023, FrASS, 10, 1289432
Bachetti, M., Rana, V., Walton, D. J., et al. 2013, ApJ, 778, 163
Brightman, M., Harrison, F., Walton, D. J., et al. 2016, ApJ, 816, 60
Brightman, M., Harrison, F. A., Fürst, F., et al. 2018, NatAs, 2, 312
Carpano, S., Haberl, F., Maitra, C., & Vasilopoulos, G. 2018, MNRAS, 476, L45
Combi, J. A., Fogantini, F. A., Saavedra, E. A., et al. 2024, A&A, 686, A121
Done, C., Gierliński, M., & Kubota, A. 2007, A&ARv, 15, 1
Earnshaw, H. M., Roberts, T. P., Heil, L. M., et al. 2016, MNRAS, 456, 3840
Earnshaw, H. P., Roberts, T. P., Middleton, M. J., Walton, D. J., & Mateos, S. 2019, MNRAS, 483, 5554
Evans, I. N., Primini, F. A., Glotfelty, C. S., et al. 2019, yCat, IX/57
Evans, P. A., Beardmore, A. P., Page, K. L., et al. 2009, MNRAS, 397, 1177
Feng, H., & Kaaret, P. 2005, ApJ, 633, 1052
Feng, H., & Kaaret, P. 2007, ApJ, 668, 941
Fürst, F., Walton, D. J., Harrison, F. A., et al. 2016, ApJL, 831, L14
Fürst, F., Walton, D. J., Heida, M., et al. 2021, A&A, 651, A75
Ghosh, T., & Rana, V. 2021, MNRAS, 504, 974
Gladstone, J. C., Roberts, T. P., & Done, C. 2009, MNRAS, 397, 1836
Heil, L. M., Vaughan, S., & Roberts, T. P. 2009, MNRAS, 397, 1061
Ingram, A., & Done, C. 2012, MNRAS, 419, 2369
Israel, G. L., Belfiore, A., Stella, L., et al. 2017, Sci, 355, 817
Kalberla, P. M. W., Burton, W. B., Hartmann, D., et al. 2005, A&A, 440, 775
Kara, E., Pinto, C., Walton, D. J., et al. 2020, MNRAS, 491, 5172
King, A., Lasota, J.-P., & Middleton, M. 2023, NewAR, 96, 101672
Kosec, P., Pinto, C., Walton, D. J., et al. 2018, MNRAS, 479, 3978
Madsen, K. K., García, J. A., Stern, D., et al. 2024, FrASS, 11, 1357834
Middleton, M. J., Brightman, M., Pintore, F., et al. 2019, MNRAS, 486, 2
Middleton, M. J., Heil, L., Pintore, F., Walton, D. J., & Roberts, T. P. 2015a, MNRAS, 447, 3243
Middleton, M. J., Roberts, T. P., Done, C., & Jackson, F. E. 2011, MNRAS, 411, 644
Middleton, M. J., Walton, D. J., Fabian, A., et al. 2015b, MNRAS, 454, 3134
Middleton, M. J., Walton, D. J., Roberts, T. P., & Heil, L. 2014, MNRAS, 438, L51
Mills, B. S., Davis, S. W., Jiang, Y.-F., & Middleton, M. J. 2023, arXiv:2304.07977
Mukherjee, E. S., Walton, D. J., Bachetti, M., et al. 2015, ApJ, 808, 64
Mushtukov, A. A., Ingram, A., Middleton, M., Nagirner, D. I., & van der Klis, M. 2019, MNRAS, 484, 687
Nasa High Energy Astrophysics Science Archive Research Center (Heasarc) 2014, HEASoft: Unified Release of FTOOLS and XANADU, Astrophysics Source Code Library, ascl:1408.004
Ng, M., Remillard, R. A., Steiner, J. F., Chakrabarty, D., & Pasham, D. R. 2022, ApJ, 940, 138
Pinto, C., Alston, W., Soria, R., et al. 2017, MNRAS, 468, 2865
Pinto, C., Middleton, M. J., & Fabian, A. C. 2016, Natur, 533, 64
Pinto, C., & Walton, D. J. 2023, arXiv:2302.00006
Pintore, F., Zampieri, L., Stella, L., et al. 2017, ApJ, 836, 113
Poutanen, J., Lipunova, G., Fabrika, S., Butkevich, A. G., & Abolmasov, P. 2007, MNRAS, 377, 1187
Rao, F., Feng, H., & Kaaret, P. 2010, ApJ, 722, 620
Ray, P. S., Guillot, S., Ho, W. C. G., et al. 2019, ApJ, 879, 130
Remillard, R. A., & McClintock, J. E. 2006, ARA&A, 44, 49
Revnivtsev, M., Churazov, E., Postnov, K., & Tsygankov, S. 2009, A&A, 507, 1211
Rodríguez Castillo, G. A., Israel, G. L., Belfiore, A., et al. 2020, ApJ, 895, 60
Sathyaprakash, R., Roberts, T. P., Walton, D. J., et al. 2019, MNRAS, 488, L35
Shakura, N. I., & Sunyaev, R. A. 1973, A&A, 24, 337
Steiner, J. F., Narayan, R., McClintock, J. E., & Ebisawa, K. 2009, PASP, 121, 1279
Stobbart, A. M., Roberts, T. P., & Wilms, J. 2006, MNRAS, 368, 397
Sutton, A. D., Roberts, T. P., & Middleton, M. J. 2013, MNRAS, 435, 1758
Sutton, A. D., Swartz, D. A., Roberts, T. P., et al. 2017, ApJ, 836, 48
Takeuchi, S., Ohsuga, K., & Mineshige, S. 2013, PASJ, 65, 88
Tully, R. B., Courtois, H. M., & Sorce, J. G. 2016, AJ, 152, 50
Urquhart, R., & Soria, R. 2016, MNRAS, 456, 1859
Walton, D. J., Bachetti, M., Fürst, F., et al. 2018a, ApJL, 857, L3
Walton, D. J., Fürst, F., Harrison, F. A., et al. 2017, ApJ, 839, 105
Walton, D. J., Fürst, F., Harrison, F. A., et al. 2018b, MNRAS, 473, 4360
Walton, D. J., Fürst, F., Heida, M., et al. 2018c, ApJ, 856, 128
Walton, D. J., Harrison, F. A., Grefenstette, B. W., et al. 2014, ApJ, 793, 21
Walton, D. J., Middleton, M. J., Rana, V., et al. 2015, ApJ, 806, 65
Walton, D. J., Pinto, C., Nowak, M., et al. 2020, MNRAS, 494, 6012
Walton, D. J., Tomsick, J. A., Madsen, K. K., et al. 2016, ApJ, 826, 87
Watarai, K.-y., Fukue, J., Takeuchi, M., & Mineshige, S. 2000, PASJ, 52, 133
Whittle, P. 1953, ArM, 2, 423
Wilkinson, T., & Uttley, P. 2009, MNRAS, 397, 666
Wilms, J., Allen, A., & McCray, R. 2000, ApJ, 542, 914